INORGANIC CHEMISTRY FRONTIERS

REVIEW

View Article Online
View Journal | View Issue

Cite this: *Inorg. Chem. Front.*, 2023, **10**, 5244

An overview of Mg-based IR nonlinear optical materials

Jia-Xiang Zhang,[a,b,c] Mao-Yin Ran,[a,b,c] Xin-Tao Wu,[a,b] Hua Lin *[a,b] and Qi-Long Zhu *[a,b]

Received 19th June 2023,
Accepted 24th July 2023

DOI: 10.1039/d3qi01144e

rsc.li/frontiers-inorganic

Infrared nonlinear optical (IR-NLO) materials play a vital role in generating IR laser output and have significant applications in the fields of communication, medicine, and security. At present, commercial IR-NLO crystals suffer from various performance drawbacks that constrain their range of applications. Therefore, the pursuit of designing and exploring new IR-NLO materials has emerged as an important avenue for the advancement of the IR laser industry. Benefiting from the various structural compositions, wide energy gaps, sufficient second-harmonic-generation intensities, strong laser-induced damage thresholds and favorable phase matching features, Mg-based IR-NLO materials have attracted wide attention in recent years. However, there has not been a specific review of this attractive family. In this overview, the recent advancements of Mg-based IR-NLO materials are summarized. These non-centrosymmetric compounds (including 36 chalcogenides and 4 pnictides) can be categorized into three types based on their chemical compositions: (i) ternary $MgGa_2Se_4$, $MgSiP_2$, $MgSiAs_2$, and $Mg_3Si_6As_8$; (ii) quaternary $Li_4MgGe_2S_7$, $Li_2Mg_2M^{III}_2S_6$ (M^{III} = Si, Ge), $AEMg_6Ga_6S_{16}$ (AE = Ca, Sr, Ba), $RE_6MgSi_2S_{14}$ (RE = Y, La–Nd, Sm, and Gd–Er), $Li_2MgM^{IV}Se_4$ (M^{IV} = Ge, Sn), $Na_4MgM^{III}_2Se_6$ (M^{III} = Si, Ge), $Cu_2MgM^{IV}Q_4$ (M^{IV} = Si, Ge; Q = S, Se), $M^{I}Mg_3M^{III}_3Q_8$ (M^{I} = Na, Cu, Ag; M^{III} = Al, Ga; Q = S, Se), and $Mg_2In_3Si_2P_7$; and (iii) quinary $Ba_6Cu_{1.9}Mg_{1.1}Ge_4S_{16}$ and $Ba_6Cu_{1.94}Mg_{1.06}Sn_4S_{16}$. Their solid-state synthesis, crystal structures, optical properties and structure–activity relationships are systematically discussed. Finally, some useful conclusions and outlooks on this topic have been put forward.

1. Introduction

Nonlinear optical (NLO) crystals are crucial components of full-state lasers as they possess the capacity to enhance the frequency range, making them applicable in a variety of aspects such as laser spectroscopy, long distance laser communication, signal processing and so on.[1–18] Due to the limitations of laser wavelength, significant research has been conducted on second order NLO materials, owing to their eminent ability to generate second harmonic generation (SHG). According to the various application bands, NLO materials can be divided into three groups, including ultraviolet (UV), visible-near infrared (Vis-NIR), mid- and far-infrared (MFIR) groups. Among them, NLO materials of UV and Vis-NIR wavelengths have already been deeply researched and commercialized in the past decades, such as $KBe_2BO_3F_2$ (KBBF),[19] β-BaB_2O_4 (β-BBO),[20] LiB_3O_5 (LBO),[21] KH_2PO_4 (KDP),[22] and $KTiOPO_4$ (KTP).[23] Although traditional commercialized IR-NLO materials, such as $AgGaS_2$,[24] $AgGaSe_2$,[25] and $ZnGeP_2$,[26] have strong SHG coefficients (d_{eff}), they still possess some inevitable drawbacks such as an imperfect laser-induced damage threshold (LIDT) of $AgGaS_2$, non-phase-matching property of $AgGaSe_2$ and negative two-photon absorption of $ZnGeP_2$.[27,28] Therefore, the development of new outstanding IR-NLO materials is not only urgent but also challenging.

In order to meet the requirements of modern laser technology, high-performance IR-NLO materials need to fulfil the following conditions: (1) suitable birefringence (Δn at the range of 0.03–0.10) for phase-matching; (2) sufficient d_{eff} (>0.5 × $AgGaS_2$, 13 pm V^{-1} for $AgGaS_2$); (3) high LIDT (>1 × $AgGaS_2$); (4) wide band gap E_g (>3.0 eV) and transparent range (covering the 3–5 μm and 8–12 μm atmospheric windows); (5) easiness to achieve growth of large size single crystals; and (6) satisfactory chemical and physical stability (mainly low hygroscopicity, resistance to the atmosphere, and possibility of cutting and grinding).[29–40] In addition to the performance requirements mentioned above, it is also imperative that the material be crystallized in a non-centrosymmetric space group. This is because it is a prerequisite for it to function as an IR-NLO

[a]*State Key Laboratory of Structural Chemistry, Fujian Institute of Research on the Structure of Matter, Chinese Academy of Sciences, Fuzhou, Fujian 350002, China. E-mail: linhua@fjirsm.ac.cn, qlzhu@fjirsm.ac.cn*
[b]*Fujian Science & Technology Innovation Laboratory for Optoelectronic Information of China, Fujian 350108, China*
[c]*University of Chinese Academy of Sciences, Beijing 100049, China*

candidate.[41–43] In recent decades, several design strategies have been developed. Among these, the most commonly used method for obtaining non-centrosymmetric structures is the introduction of various asymmetric building units (ABUs) into one structure. The common ABUs for IR-NLO materials are as follows: (i) distorted $[MQ_4]$ tetrahedra (M = main-group elements; Q = chalcogen);[44–52] (ii) $[MQ_n]$ polyhedra (M = transition-metal elements; n = 2, 3, and 4);[53–57] (iii) distorted $[REQ_n]$ polyhedra (RE = rare-earth-metal elements);[58–61] (iv) lone-pair-cation-based $[MQ_n]$ polyhedra (M = As(III), Sb(III), Bi(III), Pb(II), and Sn(II));[62–71] and (v) mixed-anion $[MO_xQ_y]$ polyhedra.[72–81]

Recently, the introduction of Mg-based ABUs into the non-centrosymmetric structures has attracted considerable interest due to the following reasons: (i) Mg possesses large electropositivity (χ = 1.31), has a high Z/R ratio of 2.8 (Z, cation charge; R, cation radius), has light atomic mass and is non-poisonous. (ii) Mg is more inclined to form stable covalent bonds with chalcogen and pnictide atoms than are Ca, Sr, and Ba, which have strong ionic properties within the same family, for example, tetrahedral $[MgQ_4]$ and $[MgP_{n4}]$ (P_n = P, As) ABUs and octahedral $[MgQ_6]$ ABUs. (iii) Due to the absence of d–d and f–f electron transitions, Mg is beneficial for obtaining wide E_g values and expanding the IR transparent region.[82–96] Moreover, highly polarizable Mg-based ABUs are helpful in maintaining strong d_{eff} and suitable Δn. However, a specific summary of non-centrosymmetric Mg-based materials has not been provided, even though they have been discovered to display excellent IR-NLO performances.

In this review, the recent advancements of Mg-based IR-NLO materials are summarized. These non-centrosymmetric compounds (including 36 chalcogenides and 4 pnictides) can be categorized into three types based on their chemical composition: (i) ternary $MgGa_2Se_4$, $MgSiP_2$, $MgSiAs_2$, and $Mg_3Si_6As_8$; (ii) quaternary $Li_4MgGe_2S_7$, $Li_2Mg_2M^{III}_2S_6$ (M^{III} = Si, Ge), $AEMg_6Ga_6S_{16}$ (AE = Ca, Sr, Ba), $Li_2MgM^{IV}Se_4$ (M^{IV} = Ge, Sn), $RE_6MgSi_2S_{14}$ (RE = Y, La–Nd, Sm, and Gd–Er), $Na_4MgM^{III}_2Se_6$ (M^{III} = Si, Ge), $Cu_2MgM^{IV}Q_4$ (M^{IV} = Si, Ge; Q = S, Se), $M^{I}Mg_3M^{III}_3Q_8$ (M^{I} = Na, Cu, Ag; M^{III} = Al, Ga; Q = S, Se), and $Mg_2In_3Si_2P_7$; and (iii) quinary $Ba_6Cu_{1.9}Mg_{1.1}Ge_4S_{16}$ and $Ba_6Cu_{1.94}Mg_{1.06}Sn_4S_{16}$. Their solid-state synthesis, crystal structures, optical properties and structure–activity relationships are systematically discussed. Finally, some useful conclusions and outlooks on this topic have been put forward.

2. The survey on Mg-based IR-NLO materials

2.1 Ternary Mg-based chalcogenides and pnictides

2.1.1 $MgGa_2Se_4$. The first defect-chalcopyrite-like Mg-based chalcogenide $MgGa_2Se_4$, with a non-centrosymmetric $I\bar{4}$ space group, was successfully designed and constructed *via* a structure prediction and experiment combined method by Li and co-workers in 2022. They used high-temperature solid-state reactions to create it, by mixing MgSe, Ga, and Se in a stoichiometric ratio of 1 : 2 : 3 at 1223 K.[82]

As shown in Fig. 1, Mg and Ga atoms both coordinate with Se atoms, forming a four-coordinated model represented by tetrahedral $[MgSe_4]$ and $[GaSe_4]$ ABUs. In the $[Ga_2Se_7]$ channel, $[MgSe_4]$ ABUs are embedded *via* corner-sharing with adjacent $[Ga1Se_4]$ and $[Ga2Se_4]$, as depicted in Fig. 1b and c, resulting in a three-dimensional (3D) defect-chalcopyrite-like structure. Furthermore, this structure can also be achieved by utilizing chalcopyrite-like $AgGaSe_2$, as depicted in Fig. 1d. When one Mg atom and one vacancy replace two Ag atoms in $AgGaSe_2$, defect-chalcopyrite-like $MgGa_2Se_4$ is produced.

The developed $MgGa_2Se_4$ possesses a wide optical E_g (*ca.* 2.96 eV), a high LIDT (*ca.* 3.0 × $AgGaS_2$), a broad transparency window (covering 3–12 μm), and a suitable phase-matching d_{eff} (*ca.* 0.9 × $AgGaS_2$@150–200 μm). Therefore, $MgGa_2Se_4$ shows great potential as an IR-NLO candidate. Additionally, theoretical calculations reveal that the strong d_{eff} of $MgGa_2Se_4$ mainly originates from the $[GaSe_4]$ ABUs and nonbonding Se 4p states, and indicate that the tetrahedral $[MgSe_4]$ ABUs can effectively broaden the E_g of chalcopyrite-like compounds.

2.1.2 $MgSiP_2$ and $MgSiAs_2$. In 2018, He's group conducted a systematic study of the electronic structures, linear and NLO

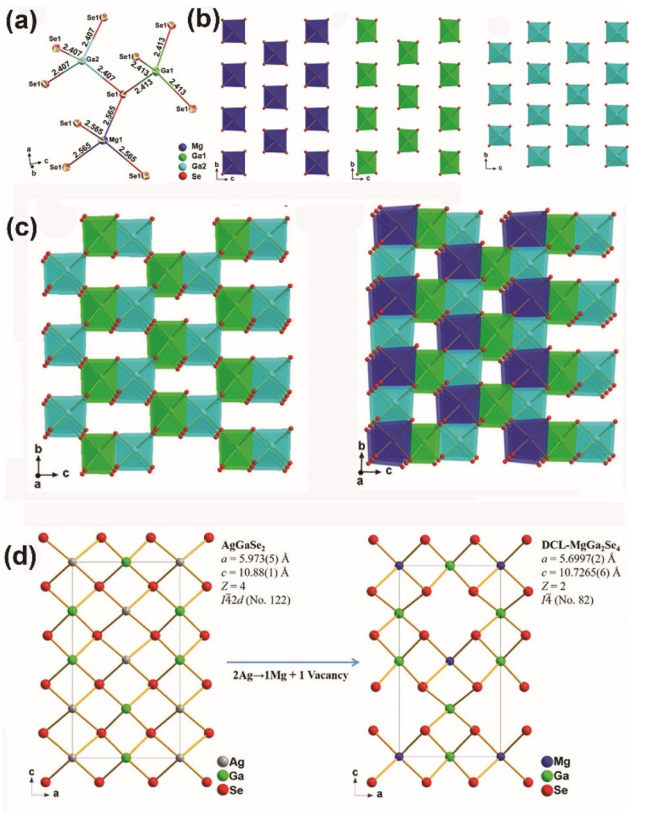

Fig. 1 (a) Coordination environment of asymmetric building units in $MgGa_2Se_4$; (b) the arrangement of isolated $[MgSe_4]$, $[Ga1Se_4]$, and $[Ga2Se_4]$ tetrahedra in the *bc* plane; (c) $[Ga_2Se_7]^{8-}$ anionic framework (left) and 3D structure of $MgGa_2Se_4$ (right); (d) structural evolution from $AgGaSe_2$ (left) to $MgGa_2Se_4$ (right). Copyright 2022 Wiley.

properties, and thermodynamic stability of the $MgM^{IV}P_{n2}$ (M^{IV} = Si, Ge, Sn; P_n = P, As) system through first-principles research. The aim of the study was to evaluate their potential in IR-NLO applications.[83] In the same year, Kovnir and his colleagues successfully synthesized $MgSiAs_2$ by reacting raw materials in the molar ratio of Mg : Si : As = 1.2 : 1 : 2 at the temperature of 1123 K.[84] To obtain a single crystal, they performed three cycles of annealing and grinding coupled with acid treatment ($HCl : H_2O$ = 1 : 1). Recently, Ye and co-workers successfully obtained millimeter-level crystals of $MgSiP_2$ (1.3 × 2.3 × 0.5 mm^3) by mixing Mg, Si, P, and $BaCl_2$ flux in a molar ratio of 1.33 : 1 : 2 : 2.67 and heating it to 1373 K.[85]

$MgSiAs_2$ and $MgSiP_2$ possess a classical chalcopyrite structure (space group: $I\bar{4}2d$), with a 3D covalent framework comprising tetrahedral [SiP_{n4}] (P_n = P, As) ABUs. The tunnels are filled with Mg^{2+} cations, which are coordinated with four closest P_n atoms (as depicted in Fig. 2). Computational and optical investigations have revealed that $MgSiAs_2$ and $MgSiP_2$ display direct E_g semiconductor properties with an optical E_g of 1.83 eV and 2.33 eV, respectively. $MgSiAs_2$ exhibits a moderate d_{eff} (*ca.* 0.6 × $AgGaS_2$@55–88 μm) and comparable LIDT (*ca.* 1.1 × $AgGaS_2$), while $MgSiP_2$ possesses a strong d_{eff} (3.5 × $AgGaS_2$@150–212 μm), and a broad IR transparency window (0.53–10.3 μm). These studies indicate that the desired balance between E_g and d_{eff} can be achieved by rationally adjusting the ionicity–covalency–metallicity properties.

2.1.3 $Mg_3Si_6As_8$. In 2018, Kovnir and co-workers reported the discovery of $Mg_3Si_6As_8$, which is the second ternary pnictide in the Mg–Si–As family. Single crystals of $Mg_3Si_6As_8$ (3 × 1.5 × 1 mm^3) were prepared through stoichiometric ratios of Mg, Si, and As and a 50 molar excess of Bi flux at 1150 K.[84] It represents a new structure type and belongs to the non-centrosymmetric $P4_332$ space group. The crystal structure of $Mg_3Si_6As_8$ is composed of a complex 3D Si–As network with interspersed Mg cations. Two distinct environments can be observed for the Mg cations: *i.e.*, tetrahedral [$MgAs_4$] and octahedral [$MgAs_6$] ABUs. Moreover, the Si–As network found in $Mg_3Si_6As_8$ is similar to that of the binary SiAs, where six As atoms surround Si–Si dumbbells in both cases. The structure of $Mg_3Si_6As_8$ creates a 3D rhombus grid fashion of Si_2@As_6 octahedra, as depicted in Fig. 3a. In contrast, these octahedra in the SiAs crystal structure form two-dimensional (2D) layers, as shown in Fig. 3b.

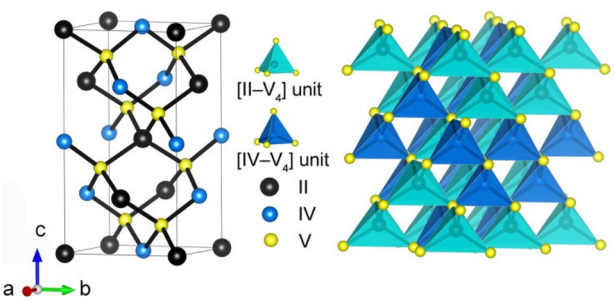

Fig. 2 Crystal structure of II–IV–V_2. Copyright 2018 IOP Publishing.

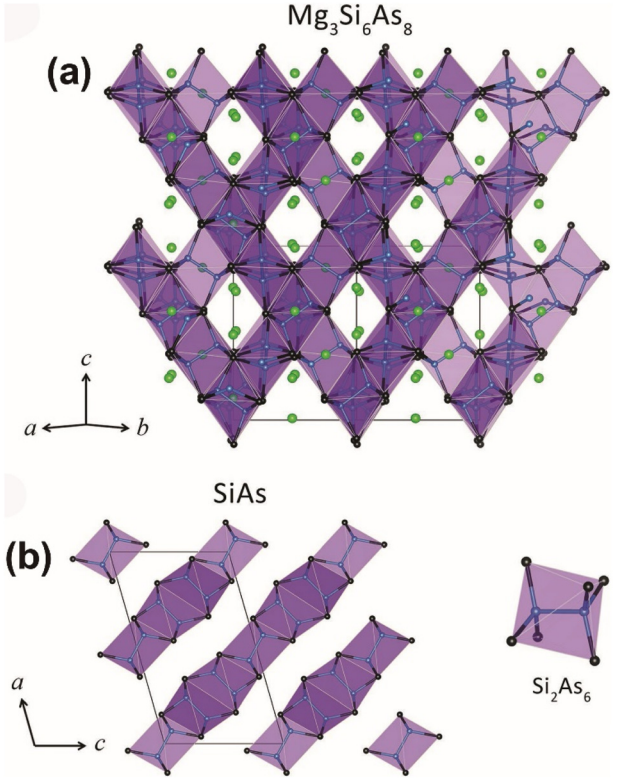

Fig. 3 (a) Crystal structure of the 3D Si–As network in $Mg_3Si_6As_8$ and (b) SiAs with Si_2@As_6 marked as purple octahedra. Green atom: Mg; blue atom: Si; black atom: As. Copyright 2018 Wiley.

$Mg_3Si_6As_8$ displays more significant thermal stability than $MgSiAs_2$ with a difference of 100 K (1240 K compared to 1140 K). Additionally, its experimental E_g is recorded as 2.02 eV. Unfortunately, it does not have SHG response due to its 432 Laue class.

2.2 Quaternary Mg-based chalcogenides and pnictides

2.2.1 $Li_4MgGe_2S_7$. The first alkali and alkaline-earth metal defect-chalcopyrite-like Mg-based chalcogenide $Li_4MgGe_2S_7$, with a monoclinic *Cc* space group, was successfully designed based on the chemical substitute-oriented strategy in the M^I_4–M^{II}–M^{IV}_2–Q_7 system by Li and co-workers in 2021.[86] Colorless block-shaped crystals of $Li_4MgGe_2S_7$ were prepared by a high-temperature solution reaction using the starting materials Li_2S, Mg, Ge, and S in the molar ratio of 2.5 : 1 : 2 : 5 at 1223 K.

Like other diamond-like chalcogenides, $Li_4MgGe_2S_7$ can be seen as a derivative of wurtzite β-ZnS.[97] Each metal is coordinated by four S atoms, forming tetrahedral [LiS_4], [MgS_4], and [GeS_4] ABUs. The six [LiS_4] ABUs are interconnected by sharing common sulfur atoms, creating a fascinating 6-membered ring (6-MR), with the [$Ge1S_4$] tetrahedron located in the middle of this unit. Furthermore, the one-dimensional (1D) [$GeMgS_5$] zigzag chains connect to the 6-MRs to construct a 2D honeycomb-like layer (Fig. 4a). The assembly of this honeycomb layer along the [101] direction is achieved *via* shared S atoms, resulting in the final 3D diamond-like framework

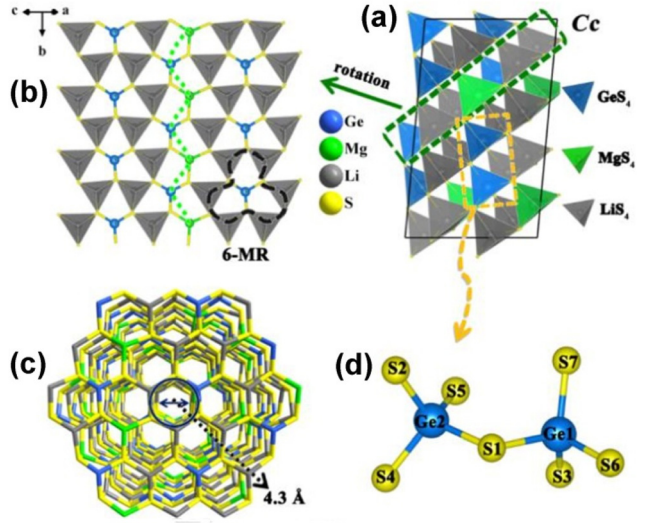

Fig. 4 Crystal structure of $Li_4MgGe_2S_7$: (a) 3D diamond-like structure; (b) single 2D layered fragment viewed along the [102] direction; (c) honeycomb-like 3D framework with an internal diameter of about 4.3 Å; (d) coordination environment of $[Ge_2S_7]^{6-}$ dimers. Copyright 2021 Wiley.

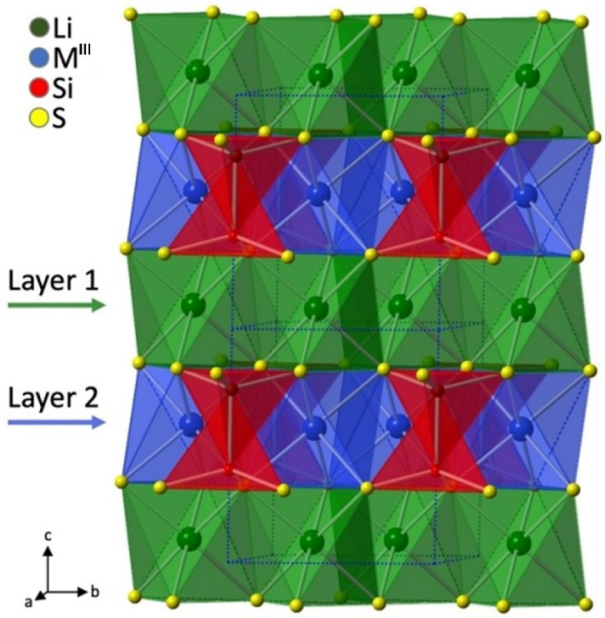

Fig. 5 Polyhedral stacking structure of $Li_2Mg_2M^{III}_2S_6$ viewed along the *bc* plane. Copyright 2022 Wiley.

(Fig. 4b). When viewed along the [203] direction, a clear depiction of the honeycomb-like 3D framework with an internal diameter of about 4.3 Å is observed (Fig. 4c). Additionally, unique $[Ge_2S_7]^{6-}$ dimers are discovered in $Li_4MgGe_2S_7$ (Fig. 4d).

The obtained $Li_4MgGe_2S_7$ exhibits the widest experimental E_g of 4.12 eV among reported quaternary metal chalcogenides. Additionally, it shows a suitable phase-matching d_{eff} (*ca.* 0.7 × $AgGaS_2$ at 2090 nm, granularity range 15–200 μm) and a high LIDT (7 × $AgGaS_2$ at 1064 nm), making it an excellent IR-NLO candidate for high-power laser applications. Theoretical calculations indicate that alkali metal Li and alkaline-earth metal Mg effectively enhance E_g, while covalent $[Ge_2S_7]^{6-}$ dimers contribute to a strong d_{eff}. This study enriches the diversity of diamond-like chalcogenides and offers a new route for the design and exploration of new IR-NLO materials with broad E_g and significant d_{eff}.

2.2.2 $Li_2Mg_2M^{III}_2S_6$ (M^{III} = Si, Ge). The first Li-containing members of the $A_{12-nx}M_x^{n+}(T_2Q_6)_2$ family, $Li_2Mg_2Si_2S_6$ and $Li_2Mg_2Ge_2S_6$, were reported by Aitken and co-workers in 2022.[87] Transparent and colorless single crystals of $Li_2Mg_2Si_2S_6$ and $Li_2Mg_2Ge_2S_6$ were obtained by the traditional high-temperature solid-phase technology using stoichiometric amounts of the reagents at 1173 K.

These two new compounds belong to the non-centrosymmetric polar space group *P*31*m* (No. 157) and represent a new structure type. As indicated in Fig. 5, each octahedral $[LiS_6]$ ABU shares its edge with three other $[LiS_6]$ ABUs to build a 2D layer in the *ab* plane, resulting in holes in the *c* direction. This layer is designated as "layer 1". Similarly, along the *c* axis, there exist nearly identical layers formed by the octahedral $[MgS_6]$ ABUs, which are subsequently referred to as "layer 2". These two layers, layer 1 and layer 2, are then interconnected along the *c* axis *via* face sharing of their respective octahedra to generate a 3D framework. These staggered ethane-like $[Si_2S_6]^{6-}$ groups are nestled within the holes present in layer 2 of the Mg–S layer, whereas the holes in layer 1 of the Li–S layer remain unoccupied. Each $[MgS_6]$ corner shares six of its corners with three ethane-like $[Si_2S_6]^{6-}$ units, and the orientation of Si–Si bonds is perpendicular to the $[MgS_6]$ layers.

The optical E_g values of $Li_2Mg_2Si_2S_6$ and $Li_2Mg_2Ge_2S_6$ have been estimated through optical diffuse reflectance spectra, which are 3.24 eV and 3.18 eV, respectively. These compounds exhibit moderate d_{eff} of approximately 0.24 × KDP and 2.9 × α-SiO_2 for $Li_2Mg_2Si_2S_6$, and 0.17 × KDP and 2.1 × α-SiO_2 for $Li_2Mg_2Ge_2S_6$ when exposed to a Nd:YAG laser at 1064 nm.

The theoretical calculation results indicate that the atomic orbitals of Li and Mg atoms do not significantly contribute to the state near the valence band maximum. This finding is significant due to their positive electrical properties and the potential interaction with the primary sulfur ions.

2.2.3 $AEMg_6Ga_6S_{16}$ (AE = Ca, Sr, Ba). The first examples of a double alkaline-earth metal chalcogenide, $AEMg_6Ga_6S_{16}$ (AE = Ca, Sr, Ba), were successfully discovered by Yu's group in 2022.[88] Millimeter-level pale-yellow crystals of $AEMg_6Ga_6S_{16}$ were prepared by the solid-state method in sealed silica tubes using the starting materials MgS, Ga_2S_3, and AES in the molar ratio 1.22 : 0.6 : 0.21 at 1323 K.

As a representative, $SrMg_6Ga_6S_{16}$ (space group: $P\bar{6}$) is adopted to describe the structure. In this structure, octahedral $[MgS_6]$ ABUs share both corners and faces to form $[Mg_3S_{14}]$ trimers, while tetrahedral $[GaS_4]$ ABUs interconnect through vertex-sharing to create two distinct kinds of 1D Ga–S chains along the *c* direction, namely, $[Ga(1)S_3]_\infty$ single chains (Fig. 6a) and $[Ga(2,3)_2S_4]_\infty$ double chains (Fig. 6b). Then, these $[Mg_3S_{14}]$

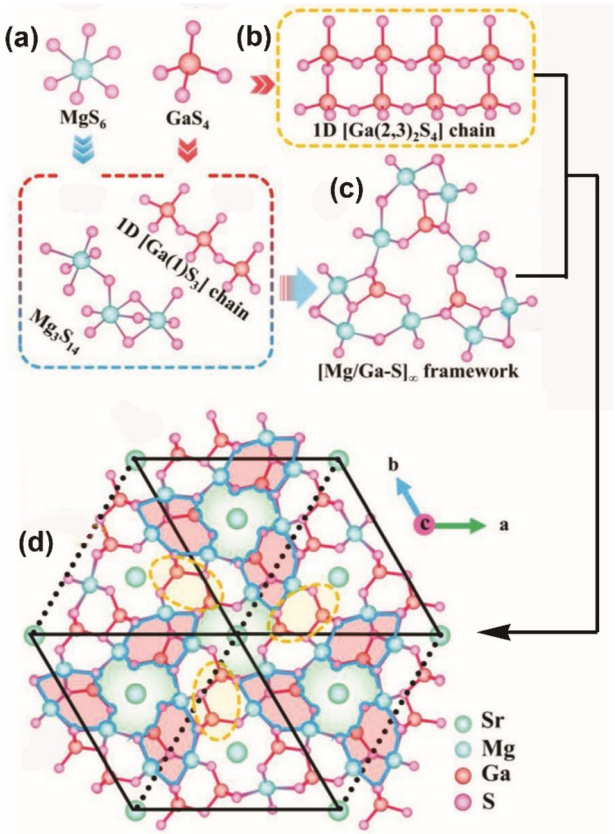

Fig. 6 (a) Coordination environment of $[Mg_3S_{14}]$ trimers and 1D $[Ga(1)S_3]$ chain; (b) 1D $[Ga(2,3)_2S_4]$ chain; (c) 3D $[(Mg/Ga)S]_\infty$ framework and (d) crystal structure of $SrMg_6Ga_6S_{16}$ viewed along the *ab* plane. Copyright 2022 Wiley.

trimers connect through vertex-sharing (in the *a*–*b* plane) and edge-sharing (along the *c*-axis) with two types of 1D Ga–S chains to form a 3D open $[Mg_6Ga_6S_{16}]^{2-}$ framework (Fig. 6c). Finally, charge-balancing Sr atoms are introduced to fill the channels of this framework (Fig. 6d).

The obtained chalcogenides melt congruently and are stable in both air and water, which facilitates the growth of single crystals. Performance characterization demonstrates that they can achieve a well-balanced combination of large phase-matching d_{eff} (*ca.* 0.7–0.8 × $AgGaS_2$ at 2090 nm, granularity range 180–250 μm), wide E_g (3.50–3.54 eV), high LIDTs (*ca.* 11 × $AgGaS_2$ at 1064 nm), and broad IR transparent windows (0.35–20 μm), which suggests that $AEMg_6Ga_6S_{16}$ are potential IR-NLO candidates. Upon further studying the structure–property relationships, it has been shown that the excellent NLO properties of the material predominantly arise from the combined contribution of the polarizable $[GaS_4]$ and $[MgS_6]$ ABUs in the 3D open $[Mg_6Ga_6S_{16}]^{2-}$ framework. These findings offer a brand-new family for developing IR-NLO candidates with stable framework structures and excellent properties.

2.2.4 $RE_6MgSi_2S_{14}$ (RE = Y, La–Nd, Sm, and Gd–Er). $RE_6MgSi_2S_7$ (RE = Y, La–Nd, Sm, and Gd–Er) with a NCS $P6_3$ space group were systematically researched by zur Loye's group in 2023.[89] With the exception of $La_6MgSi_2S_7$,[98] these compounds were all discovered for the first time. These compounds were synthesized by the flux method and crystallized by combining the boron chalcogen mixture method[99] and the molten flux method.

The crystal structure of $RE_3Mg_{0.5}SiS_7$ contains three types of olyhedral: $[MgS_6]$, $[SiS_4]$, and $[RES_8]$. The 3D structure (Fig. 7a) is constructed from bi-capped trigonal prisms of $[RES_8]$, which are shared at the edges and corners to produce a ring-shaped arrangement (Fig. 7b). Isolated $[SiS_4]$ tetrahedra (Fig. 7c) are distributed throughout the structure, positioned between the ring-shaped $[RES_8]$ assemblies (Fig. 7d). Furthermore, face-sharing $[MgS_6]$ octahedra are situated centrally within each ring arrangement and interact with their neighbouring assemblies.

The experimental values for $RE_3Mg_{0.5}SiS_7$ are an E_g of 2.77 eV and an approximate d_{eff} of 0.16 × KDP at a wavelength of 1064 nm. However, the SHG activity was not tested in any other samples due to difficulties in measuring it arising from crystal colouration in other compositions.

2.2.5 $Li_2MgM^{IV}Se_4$ (M^{IV} = Ge, Sn). Two new diamond-like chalcogenides with the formula of $Li_2MgM^{IV}Se_4$ (M^{IV} = Ge, Sn) have been reported by Pan and co-workers in 2021.[90] Both of them adopt the NCS space group of $Pmn2_1$ and were synthesized by direct combination of the stoichiometric elements at 1153 K. As depicted in Fig. 8, all of the ions within the structures occupy general sites and exhibit tetrahedral coordination models. The 3D diamond-like framework of $Li_2MgM^{IV}Se_4$ is formed by tetrahedral $[(Li/Mg)Se_4]$ $[LiSe_4]$ and $[M^{IV}Se_4]$ ABUs through corner-sharing Se atoms (Fig. 8a and c). For both compounds, there are similar channel-like structures with a channel diameter of approximately 6 Å on the *ab* direction, as given in Fig. 8b and d.

The calculated results suggest that the d_{33} of $Li_2MgSnSe_4$ and $Li_2MgGeSe_4$ are 12.19 and 14.77 pm V^{-1}, respectively,

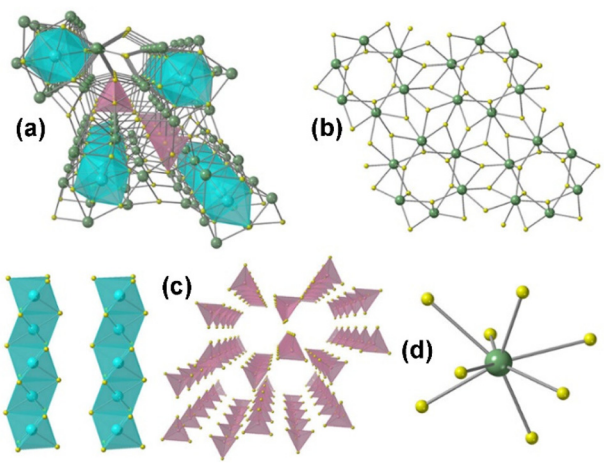

Fig. 7 (a) Crystal structure of $RE_6MgSi_2S_{14}$ from the *c*-axis; coordination environment of (b) 3D RE-S network, (c) 1D chains of face-sharing $[MgS_6]$ octahedra (left) and isolated $[GeS_4]$ tetrahedra (right), and (d) $[RES_8]$ polyhedron. Copyright 2023 American Chemistry Society.

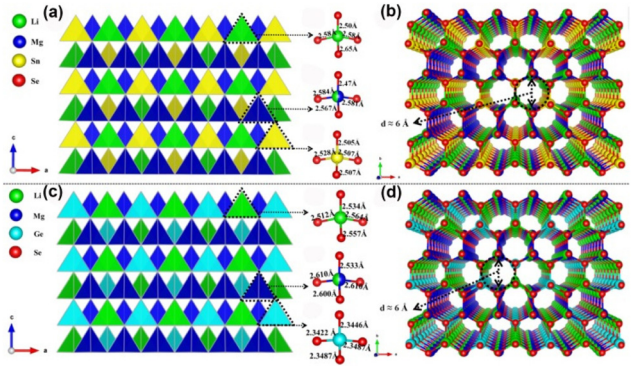

Fig. 8 Crystal structure of $Li_2MgM^{IV}Se_4$ (M^{IV} = Ge, Sn): (a and c) 3D diamond-like structures viewed along the *c* direction; (b and d) 3D channel-like structures viewed along the *ab* plane.

which primarily stem from the tetrahedral $[M^{IV}Se_4]$ ABUs and are comparable to that of the widely accepted reference material $AgGaS_2$ (d_{14} = 13.7 pm V^{-1}). The calculated E_g for $Li_2MgSnSe_4$ and $Li_2MgGeSe_4$ was 2.42 and 2.44 eV, correspondingly. Notably, these two selenides represent the first series in the M^I_2–M^{II}–M^{IV}–Q_4 system to feature alkali and alkaline-earth metals, thereby expanding the variety of structures found among diamond-like chalcogenides.

2.2.6 $Na_4MgM^{III}_2Se_6$ (M^{III} = Si, Ge). $Na_4MgM^{III}_2Se_6$ (M^{III} = Si, Ge), with a *C*2 non-centrosymmetric space group, were first reported by Pan's group in 2015.[91] They were discovered using traditional solid-state reactions with reaction materials Na, Mg, M^{III}, Ge in a molar ratio of 4 : 1 : 2 : 6 at 973 K (for $Na_4MgSi_2Se_6$) and 873 K (for $Na_4MgGe_2Se_6$).

Due to their similar structures, $Na_4MgSi_2Se_6$ has been chosen as the representative. The Mg atoms are coordinated with six Se atoms to generate octahedral $[MgSe_6]$ ABUs, which are then connected with $[Si_2Se_6]$ ABUs to build a 2D layered structure. Finally, charge-balancing Na^+ cations fill the channels and interlayer spaces to further form a 3D framework (Fig. 9a). When compared to the formerly reported $Na_8Pb_2(Si_2Se_6)_2$ (Fig. 9b),[100] which also owns the same ethane-like $[Si_2Se_6]$ dimers, a significant difference occurs in their different space groups (*C*2/*m vs. C*2).

Significantly, they display high power LIDTs of 9 and 7 times that of $AgGaS_2$, moderate phase-matching d_{eff} of 0.5 and 1.3 times that of $AgGaS_2$ within the particle size range of 150–200 μm, and wide IR transmission windows of 0.45–20 μm. These properties could potentially remove the key drawbacks, such as small LIDTs and harmful TPA, observed in commercially available IR-NLO crystals. Based on the calculation results, that calculated Δn values are close to 0.10 for $Na_4MgM^{III}_2Se_6$ at the wavelength of 1064 nm and the charge transitions from Se 4p, M^{III} 3p/4p and Mg 2p play the important role for d_{eff}.

2.2.7 $Cu_2MgM^{IV}Q_4$ (M^{IV} = Si, Ge; Q = S, Se). Three new diamond-like chalcogenides with the formula $Cu_2MgM^{IV}Q_4$ (M^{IV} = Si, Ge; Q = S, Se) have been obtained by the traditional high-temperature solid-state method by Guo and co-workers in 2013.[92] All of them belong to the non-centrosymmetric space group of $Pmn2_1$ in the wurtzite-type superstructure and synthesized by direct combination of the stoichiometric elements at 1223 K. As depicted in Fig. 10, all of the ions within the structures occupy general sites and exhibit tetrahedral coordination models. Each Q^{2-} anion is tetrahedrally coordinated with one Mg^{2+} cation, one M^{4+} cation, and two Cu^+ cations, resulting in a 3D honeycomb structure. The remarkable structural characteristic of $Cu_2MgM^{IV}Q_4$ is the introduction of a tetrahedrally coordinated Mg^{2+} cation to the M^{II} sites of diamond-like chalcogenides with the formula M^I_2–M^{II}–M^{IV}–Q_4 (where M^I = group 11 metals and Li; M^{II} = group 12 metals; M^{IV} = group 14 metals; Q = S, Se).

The experimental E_g were determined to be 3.20 and 2.36 eV for Cu_2MgSiS_4 and Cu_2MgGeS_4, respectively. Although both of them belong to the non-centrosymmetric space group, no noticeable SHG response was observed when testing a modified /Kurtz-NLO system with 1064 and 2100 nm laser radiation.

2.2.8 $M^IMg_3M^{III}_3Q_8$ (M^I = Na, Cu, Ag; M^{III} = Al, Ga; Q = S, Se). $M^IMg_3M^{III}_3Q_8$ (M^I = Na, Cu, Ag; M^{III} = Al, Ga; Q = S, Se) represents a newly discovered quaternary chalcogenide family within the M^I_2Q–$M^{II}Q$–$M^{III}_2Q_3$ system. These 9 materials constitute the first series discovered in this family by Li and co-workers in 2022.[93] The $NaMg_3Ga_3Q_8$, $NaMg_3Al_3Q_8$ and

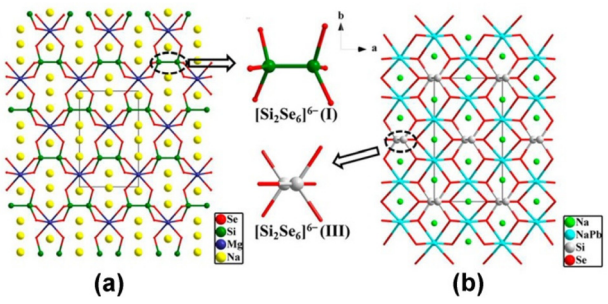

Fig. 9 Crystal structures of (a) $Na_4MgSi_2Se_6$ and (b) $Na_8Pb_2(Si_2Se_6)_2$ viewed along the *ab* plane. Copyright 2015 American Chemistry Society.

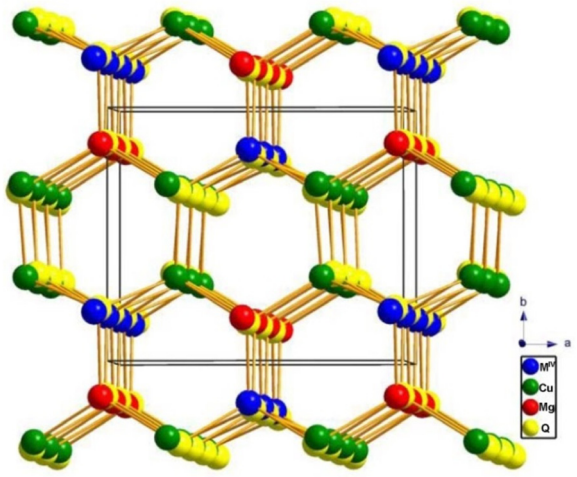

Fig. 10 3D diamond-like structure of $Cu_2MgM^{IV}Q_4$ viewed slightly along the *c* direction. Copyright 2013 Elsevier.

$CuMg_3Ga_3S_8$ compounds were synthesized utilizing a flux method. The necessary initial reactant, Na/Cu, Mg, and Ga/Al, along with S/Se, were used in a molar ratio of 2 : 3 : 3 : 8. The synthesis process was carried out at a temperature of 1273 K. For the $AgMg_3Ga_3Q_8$ and $LiMg_3Ga_3Q_8$ compounds, the same method was applied; however, Ga_2O_3 replaced Ga as the raw material.

Given that $M^{I}Mg_3M^{III}_3Q_8$ adopt the same non-centrosymmetric $P\bar{6}$ space group and exhibit similar structural features, $AgMg_3Ga_3S_8$ has been chosen as the representative. The S atoms are coordinated with Mg, Ga and Ag atoms to form octahedral $[MgS_6]$, tetrahedral $[GaS_4]$ and triangle-planar $[AgS_3]$ ABUs (Fig. 11a). Interestingly, diverse connection modes such as vertex-, edge-, and face-sharing between these ABUs can be found in this structure. For example, $[GaS_4]$ ABUs interconnect to form 1D $[GaS_4]_\infty$ and $[Ga_2S_7]_\infty$ *via* corner-sharing. Meanwhile, $[MgS_6]$ ABUs connect together to construct 1D $[MgS_6]_\infty$ and $[Mg_2S_9]_\infty$ chains *via* edge- or/and face-sharing (Fig. 11b). Moreover, the resulting 1D $[GaS_4]_\infty$ and $[MgS_6]_\infty$ chains arrange alternately by vertex-sharing, creating a distinctive windmill-like $[Mg_3Ga_3S_{24}]$ unit (Fig. 11c). Finally, the $[Mg_3Ga_3S_{24}]$ units are linked by the 1D $[Ga_2S_7]_\infty$ and $[Mg_2S_9]_\infty$ chains, and the Ag atoms are positioned in the interior of the $[Mg_3Ga_3S_{24}]$ channels, forming the 3D framework of $AgMg_3Ga_3S_8$ (Fig. 11d). Compared to the $[Ga_6S_{18}]$ unit in $AgGaS_2$, the $[Mg_3Ga_3S_{24}]$ unit is formed by replacing three *meta*-position $[GaS_4]$ ABUs with three $[MgS_6]$ ABUs (Fig. 11d).

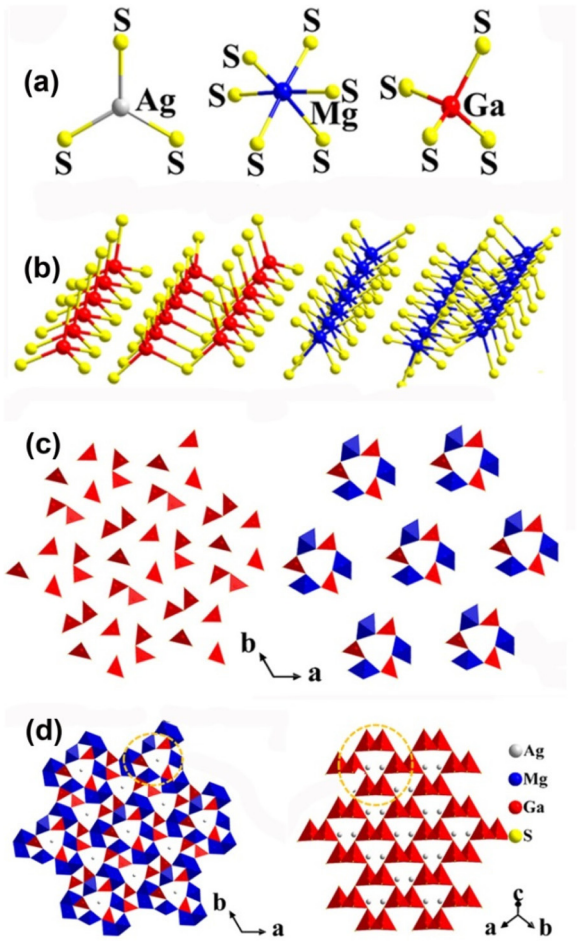

Fig. 11 (a) Coordinated environment of $[AgS_3]$, $[MgS_6]$, and $[GaS_4]$ atoms; (b) 1D $[GaS_4]$, $[Ga_2S_7]$, $[MgS_6]$, and $[Mg_2S_9]$ chains; (c) 1D Ga–S chains and $[Mg_3Ga_3S_{24}]$ groups viewed along the *ab* plane; (d) 3D structure of $AgMg_3Ga_3S_8$ (left) and $AgGaS_2$ (right) with the $[Ga_6S_{18}]$ units marked (yellow dashed circle). Copyright 2022 American Chemistry Society.

The experimental results suggest that $NaMg_3Ga_3Se_8$ has potential as an IR-NLO candidate due to its sufficient d_{eff} (~1 × $AgGaS_2$@180–212 μm), wide selenide E_g (2.77 eV), suitable Δn (0.079@546 nm), and large LIDT (~2.3 × $AgGaS_2$). Moreover, the SHG-density maps indicate that the large d_{eff} in $NaMg_3Ga_3Se_8$ is mainly provided by the NLO-active $[GaSe_4]$ ABUs. Besides, the optical and NLO parameters of other compounds are presented in Table 1.

2.2.9 $Mg_2In_3Si_2P_7$. By implementing a "rigidity-flexibility coupling" approach, a quaternary Mg-based phosphide $Mg_2In_3Si_2P_7$ was successfully discovered by Ye's group in 2021.[94] Millimeter-level red crystals of $Mg_2In_3Si_2P_7$ (2.5 × 1.5 × 0.5 mm^3) were obtained by the solid-state method in sealed silica tubes using the starting materials of Mg, In, Si, P and flux $BaBr_2$ in the molar ratio of 1.33 : 1.5 : 1 : 3.5 : 2.67 at 1073 K.

The $Mg_2In_3Si_2P_7$ crystal structure displays a diamond-like pattern, which is created by the vertex-sharing $[(Mg/In)P_4]$, $[(In/Si)P_4]$ and $[SiP_4]$ ABUs (Fig. 12a). The tetrahedral $[SiP_4]$ ABUs are integrated into the 12-MR rings of $[(Mg/In)_6P_6]$, thereby generating 1D $[(Mg/In)_6SiP_{16}]_\infty$ chains (Fig. 12a), and the tetrahedral $[(In/Si)P_4]$ ABUs interlink through corner-sharing and form zigzag 1D $[(In/Si)P_3]_\infty$ chains. These two kinds of 1D chains are interconnected to build 2D layers (Fig. 12b), which are arranged in an *ABAB* fashion, giving rise to a 3D polar structure (Fig. 12a). Additionally, $Mg_2In_3Si_2P_7$ exhibits a hexagonal close-packed structure that closely resembles wurtzite (Fig. 12c), which was confirmed by the experimental results of the selected area electron diffraction patterns (Fig. 12d).

Noticeably, $Mg_2In_3Si_2P_7$ has achieved rare coexistence of huge d_{eff} (2 × $ZnGeP_2$ and 7.1 × $AgGaS_2$, granularity range 150–212 μm), a sufficient E_g of 2.21 eV, a large Δn of 0.107, and a wide IR transparent window of 0.56–16.4 μm. Theoretical calculations have revealed that the colossal d_{eff} and large Δn can be attributed to the favorable arrangement of tetrahedral $[InP_4]$ and $[SiP_4]$ ABUs. These findings not only open up a new route for sophisticated IR-NLO crystal design but also have the potential to inspire more discoveries in the quaternary diamond-like families.

2.3 Quinary Mg-based chalcogenides

2.3.1 $Ba_6Cu_{1.9}Mg_{1.1}Ge_4S_{16}$ and $Ba_6Cu_{1.94}Mg_{1.06}Sn_4S_{16}$. $Ba_6Cu_{1.9}Mg_{1.1}Ge_4S_{16}$ and $Ba_6Cu_{1.94}Mg_{1.06}Sn_4S_{16}$ were reported by Wang's group in 2021 and 2022, respectively.[95,96] Both of them can be obtained through the traditional high-temperature solid-state method using the stoichiometric amounts of the reagents at 1073 K, with the difference being that the

Table 1 A summary of reported Mg-based IR-NLO materials

Compound	Mg polyhedron	Unit cell	Space group	E_g [a] (eV)	Window of transparence (μm)	d_{eff} [b]	LIDT[b]	Δn[c]	PM/NPM[d]	Ref.
$MgGa_2Se_4$	$MgSe_4$	Tetragonal	$I\bar{4}$	2.96	1.35–12.43	0.9 × $AgGaS_2$ (@2.09 μm)	3.0 × $AgGaS_2$	0.048 (@0.55 μm)	PM	82
$MgSiP_2$	MgP_4	Tetragonal	$I\bar{4}2d$	2.34	0.53–10.3	3.5 × $AgGaS_2$ (@2.05 μm)	N/A[e]	N/A	PM	84
$MgSiAs_2$	$MgAs_4$	Tetragonal	$I\bar{4}2d$	1.83	N/A	0.6 × $AgGaS_2$ (@2.09 μm)	1.12 × $AgGaS_2$	N/A	PM	85
$Li_4MgGe_2S_7$	MgS_4	Monoclinic	Cc	4.12	N/A	0.7 × $AgGaS_2$ (@2.09 μm)	7.0 × $AgGaS_2$	0.035 (@1.06 μm) (exp.)	PM	86
$Li_2Mg_2Si_2S_6$	MgS_6	Trigonal	$P31m$	3.24	N/A	0.3 × KDP (@1.06 μm)	N/A	N/A	N/A	87
$Li_2Mg_2Ge_2S_6$	MgS_6	Trigonal	$P31m$	3.18	N/A	0.2 × KDP (@1.06 μm)	N/A	N/A	N/A	87
$CaMg_6Ga_6S_{16}$	MgS_6	Hexagonal	$P\bar{6}$	3.54	0.35–20	0.7 × $AgGaS_2$ (@2.09 μm)	11.7 × $AgGaS_2$	0.046 (@1.06 μm) (exp.)	PM	88
$SrMg_6Ga_6S_{16}$	MgS_6	Hexagonal	$P\bar{6}$	3.51	0.35–20	0.7 × $AgGaS_2$ (@2.09 μm)	11.5 × $AgGaS_2$	0.042 (@1.06 μm) (exp.)	PM	88
$BaMg_6Ga_6S_{16}$	MgS_6	Hexagonal	$P\bar{6}$	3.50	0.35–20	0.7 × $AgGaS_2$ (@2.09 μm)	11.5 × $AgGaS_2$	0.041 (@1.06 μm) (exp.)	PM	88
$Gd_6MgGe_2S_{14}$	MgS_6	Hexagonal	$P6_3$	2.77	N/A	0.2 × KDP (@1.06 μm)	N/A	N/A	N/A	89
$Li_2MgGeSe_4$	(Li/Mg)Se_4	Orthorhombic	$Pmn2_1$	2.44 (cal.)	N/A	d_{33} = 12.19 pm V^{-1} (cal.)	N/A	0.012 (@1.06 μm)	N/A	90
$Li_2MgSnSe_4$	(Li/Mg)Se_4	Orthorhombic	$Pmn2_1$	2.62	N/A	d_{33} = 14.77 pm V^{-1} (cal.)	N/A	0.011 (@1.06 μm)	N/A	90
$Na_4MgSi_2Se_6$	$MgSe_6$	Monoclinic	$C2$	2.53	0.45–20	0.5 × $AgGaS_2$ (@2.09 μm)	9.0 × $AgGaS_2$	0.100 (@1 μm)	PM	91
$Na_4MgGe_2Se_6$	$MgSe_6$	Monoclinic	$C2$	2.85	0.45–20	1.3 × $AgGaS_2$ (@2.09 μm)	7.0 × $AgGaS_2$	0.092 (@1 μm)	PM	91
$AgMg_3Ga_3S_8$	MgS_6	Hexagonal	$P\bar{6}$	3.59	N/A	d_{11} = 3.74 pm V^{-1} (cal.)	N/A	0.091 (@1.06 μm)	N/A	93
$AgMg_3Ga_3Se_8$	MgS_6	Hexagonal	$P\bar{6}$	2.43 (cal.)	N/A	d_{11} = 10.2 pm V^{-1} (cal.)	N/A	0.17 (@1.06 μm)	N/A	93
$NaMg_3Ga_3S_8$	MgS_6	Hexagonal	$P\bar{6}$	3.70	N/A	d_{11} = 3.24 pm V^{-1} (cal.)	N/A	0.030 (@1.06 μm)	N/A	93
$NaMg_3Ga_3Se_8$	$MgSe_6$	Hexagonal	$P\bar{6}$	2.77	N/A	1.0 × AGS (@2.09 μm)	2.3 × $AgGaS_2$	0.079 (@0.55 μm) (exp.)	PM	93
$NaMg_3Al_3S_8$	MgS_6	Hexagonal	$P\bar{6}$	4.20	N/A	d_{11} = 2.45 pm V^{-1}	N/A	0.010 (@1.06 μm)	N/A	93
$NaMg_3Al_3Se_8$	MgS_6	Hexagonal	$P\bar{6}$	3.72 (cal.)	N/A	d_{11} = 3.93 pm V^{-1}	N/A	0.038 (@1.06 μm)	N/A	93
$Mg_2In_3Si_2P_7$	(In/Mg)P_4	Monoclinic	$P2_1$	2.21	0.56–16.4	7.1 × $AgGaS_2$ (@2.05 μm)	N/A	0.107 (@2.05 μm)	PM	94
$Ba_6Cu_{1.9}Mg_{1.1}Ge_4S_{16}$	(Cu/Mg)S_4	Cubic	$I\bar{4}3d$	2.92	N/A	2.3 × $AgGaS_2$ (@2.09 μm)	6.2 × $AgGaS_2$	N/A	NPM	95
$Ba_6Cu_{1.9}Mg_{1.1}Sn_4S_{16}$	(Cu/Mg)S_4	Cubic	$I\bar{4}3d$	2.4	N/A	2.5 × $AgGaS_2$ (@2.09 μm)	2.5 × $AgGaS_2$	N/A	NPM	96

[a] Experimental value. [b] Powder sample. [c] Theoretical value. [d] PM = phase-matchability, NPM = nonphase-matchability. [e] N/A = not available.

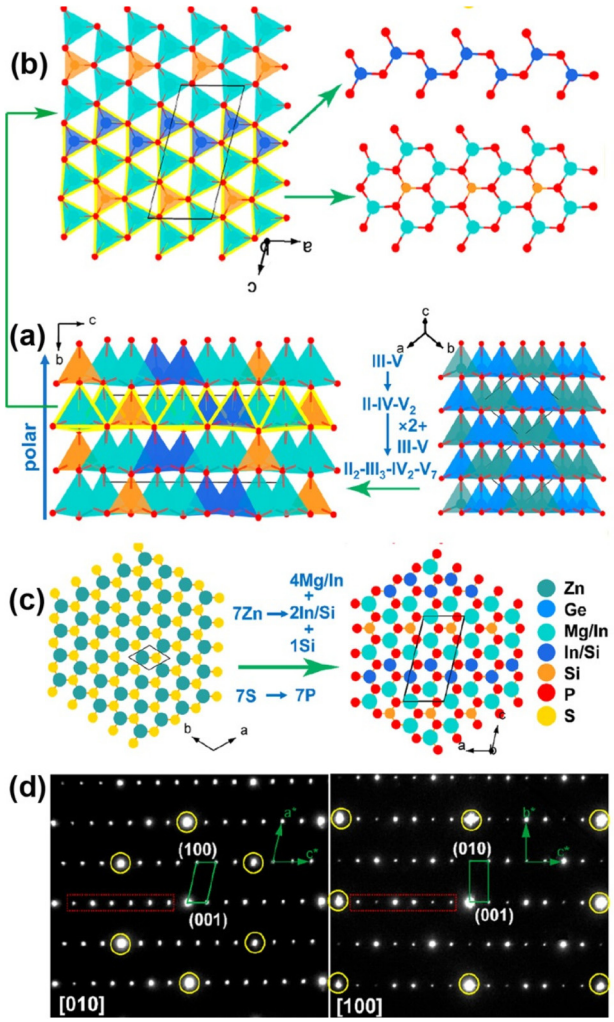

Fig. 12 (a) Structural evolution from $ZnGeP_2$ (right) to $Mg_2In_3Si_2P_7$ (left); (b) single 2D tetrahedral-stacking layer composed of 1D [(Mg/In)$_6$SiP$_{16}$] and [In/SiP$_3$] chains in $Mg_2In_3Si_2P_7$. (c) Structural evolution from wurtzite ZnS (left) to $Mg_2In_3Si_2P_7$ (right); (d) electron diffraction patterns of $Mg_2In_3Si_2P_7$ along the [010] and [100] zone axes. Copyright 2021 American Chemistry Society.

former requires the use of KI salt as the flux, while the latter does not.

$Ba_6Cu_{1.9}Mg_{1.1}Ge_4S_{16}$ and $Ba_6Cu_{1.94}Mg_{1.06}Sn_4S_{16}$ are both members of the $M^{II}_6M^{I}_4M^{IV}_4Q_{16}$ (M^{II} = Sr, Ba; M^{I} = Li, Cu, Ag; M^{IV} = Ge, Sn; Ch = S, Se) family.[101,102] These two compounds feature mixed locations at the Li/Cu/Ag atomic sites, where M^{I} metals are replaced by M^{II} metals. Since both compounds belong to the same non-centrosymmetric $I\bar{4}3d$ space group and exhibit similar structural features, $Ba_6Cu_{1.9}Mg_{1.1}Ge_4S_{16}$ has been chosen as the representative. The 3D framework is formed by tetrahedral [(Cu/Mg)S$_4$] and [GeS$_4$] ABUs through corner-sharing S atoms, where the charge-balanced Ba^{2+} packing in the empty spaces. The polyhedral and ball–stick modes of $Ba_6Cu_{1.9}Mg_{1.1}Ge_4S_{16}$ are displayed in Fig. 13a and b, respectively. Besides, the coordination environment between the tetrahedral [(Cu/Mg)S$_4$] and [GeS$_4$] ABUs is highlighted in Fig. 13c.

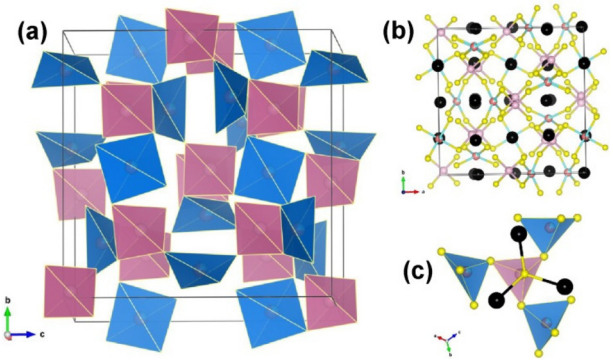

Fig. 13 Crystal structural of $Ba_6Cu_{1.9}Mg_{1.1}Sn_4S_{16}$: (a) polyhedral packing model; (b) ball-and-stick model; (c) coordination environment of [(Cu/Mg)S$_4$] (pink) and [SnS$_4$] (blue) tetrahedra. Black: Ba; red: Mg; blue: Cu; pink: Sn; yellow: S. Copyright 2021 American Chemistry Society.

The experimental E_g was determined to be 2.92 and 2.24 eV for $Ba_6Cu_{1.9}Mg_{1.1}Ge_4S_{16}$ and $Ba_6Cu_{1.94}Mg_{1.06}Sn_4S_{16}$, respectively. Through the placement of monovalent Cu^+ with divalent Mg^{2+}, the optical properties can be shifted to promote a good balance between d_{eff} and LIDT. For instance, $Ba_6Cu_{1.9}Mg_{1.1}Ge_4S_{16}$ possesses a strong non-phase-matching d_{eff} and a high LIDT of 2.3 × $AgGaS_2$ and 6.2 × $AgGaS_2$ within the particle size range of 28–55 μm, respectively. Theoretical calculations confirmed that the [(Cu/Mg)S$_4$] and [GeS$_4$] ABUs are the major role of the SHG responses.

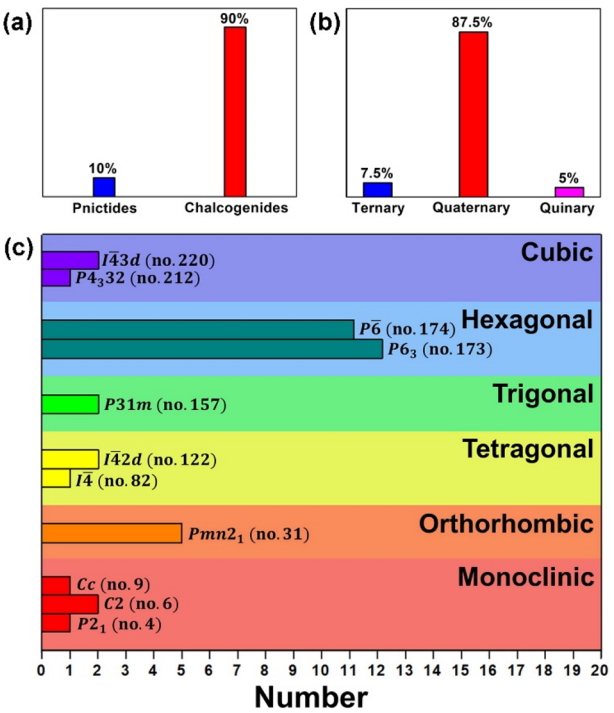

Fig. 14 Distributions of the Mg-based IR-NLO materials according to (a) material type, (b) chemical component and (c) the space groups in different crystal systems.

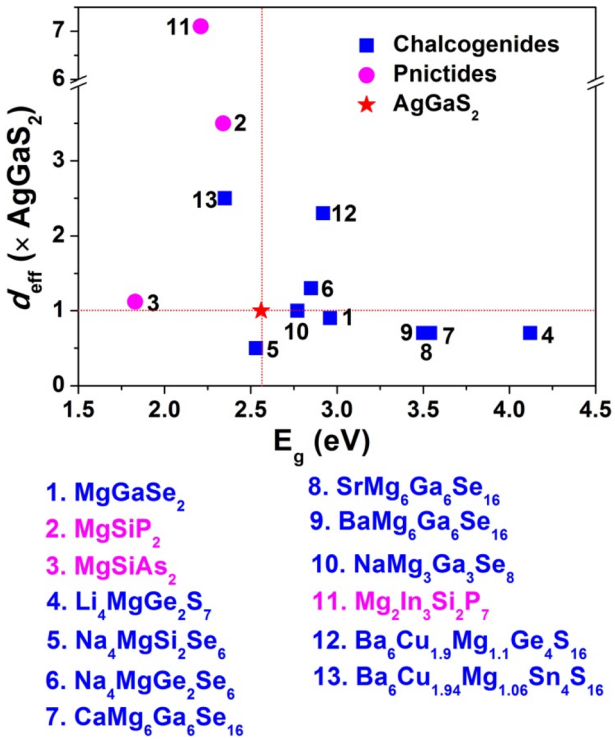

Fig. 15 Comparison of the d_{eff} (× AGS) and E_g (eV) for selected Mg-based materials with IR NLO properties.

3. Conclusions and perspectives

Research interest in new IR-NLO candidates has stimulated the rapid development of new NCS Mg-based chalcogenides and pnictides. In this review, we presented a brief introduction to the solid-state synthesis, structural design, and NLO properties together with the structure–property relationship of the recently reported Mg-based IR-NLO materials. The distribution of E_g (eV) in relation to d_{eff} (× $AgGaS_2$) and detailed performance comparison for previously reported Mg-based IR-NLO materials are illustrated in Fig. 14, 15 and Table 1, respectively. From this, certain characteristics can be inferred:

(i) The currently reported Mg-based IR-NLO materials (including 36 chalcogenides and 4 pnictides) are mainly quaternary compounds (87.5%), with a small amount of ternary (7.5%) and pentagonal (5%) compounds (Fig. 14a and b). Moreover, they mainly belong to the highly symmetrical crystal systems, such as the hexagonal space group of $P6_3$ (27.5%) and $P\bar{6}$ (30%) (Fig. 14c).

(ii) The Mg-based compounds mentioned above are synthesized using traditional high-temperature solid-state methods. Some of them require the use of fluxes to assist in the reaction, including Bi, NaCl, NaI, KI, CsCl, $CaCl_2$, $BaCl_2$, and $BaBr_2$. Furthermore, it is worth noting the synthesis of $RE_6MgSi_2S_{14}$, which utilizes a boron chalcogen mixture method. It is anticipated that this method can be expanded to other chalcogenide systems, allowing for the exploration of further captivating physical properties.

(iii) As displayed in Fig. 15, most of them are stronger than commercial $AgGaS_2$ (E_g = 2.56 eV and d_{eff} = 1 × $AgGaS_2$). Remarkably, quaternary pnictide $Mg_2In_3Si_2P_7$ exhibits the largest d_{eff} (7.1 × $AgGaS_2$) due to the most favorable combination and arrangement of ABUs, while $NaMg_3Al_3S_8$ possesses the widest E_g of 4.20 eV in this system.

(iv) Due to the incompatibility of optical parameters, there are currently no reports of IR-NLO Mg-based materials that can achieve a balance between large E_g (>3.0 eV) and strong phase-matching d_{eff} (>1.0 × $AgGaS_2$).

Many distinguished researchers have made significant contributions in exploring and verifying the potential of Mg-based IR NLO materials. However, more research is required to fully uncover the potential of these materials. Some possible avenues for further progress are outlined below:

(1) The pnictide system shows promise for further exploration. However, only a few Mg-based pnictides have been reported, and their usability has been limited by their narrow E_g. To increase the E_g, an effective solution could be to introduce high electronegativity "structure scissors" ions, such as alkali metals, alkaline earth metals, and halogens.

(2) Efforts are underway to synthesize high-performance Mg-based IR-NLO compounds by combining other ABUs. Currently, distorted [MQ_4] tetrahedra (M = group 13 and 14 metal elements) are the most commonly used second ABUs, but it would be worthwhile to experiment with introducing other ABUs, such as, lone-pair-cation-based [MQ_n] ABUs, distorted [REQ_n] ABUs, or mixed-anion [MO_xQ_y] ABUs.

(3) The theoretical calculation system for IR-NLO materials requires further study. Researchers can gain crucial properties through first-principles calculations, reducing the experimental blind spots and deepening the understanding of structure–activity relationships. Due to the development of anionic group theory in the research of oxide systems, there is still a significant difference between the calculation results and single crystal tests when applied to chalcogenides and pnictides. Therefore, there is an urgent need to establish a theoretical system that is suitable for IR-NLO materials.

(4) The study of large-sized crystal growth still requires further enhancement. After identifying crystals with exceptional properties, it is crucial for their scientific and technological development to investigate the possibility of growing them into large-sized crystals for commercial purposes.

Author contributions

Jia-Xiang Zhang: investigation and writing – original draft. Mao-Yin Ran: investigation and formal analysis. Xin-Tao Wu: conceptualization and formal analysis. Hua Lin: supervision, conceptualization and writing – review and editing. Qi-Long Zhu: supervision and writing – review and editing.

Conflicts of interest

There are no conflicts to declare.

Acknowledgements

This work was sponsored by the National Natural Science Foundation of China (21771179), Fujian Science & Technology Innovation Laboratory for Optoelectronic Information of China (2021ZR118), and the Natural Science Foundation of Fujian Province (2022L3092 and 2023H0041).

References

1 U. Keller, Recent developments in compact ultrafast lasers, *Nature*, 2003, **424**, 831–838.
2 T. Schneider, *Nonlinear optics in telecommunications*, Springer Science & Business Media, 2004.
3 D. N. Nikogosyan, *Nonlinear Optical Crystals: A Complete Survey*, Springer, New York, 1st edn, 2005.
4 F. J. Duarte, *Tunable Laser Applications*, CRC Press, Boca Raton, 2008.
5 V. A. Serebryakov, E. V. Boiko, N. N. Petrishchev and A. V. Yan, Medical applications of mid-TR lasers: problems and prospects, *J. Opt. Technol.*, 2010, **77**, 6–17.
6 Structure-Property Relationships in Nonlinear Optical Crystals II The IR Region, in *Structure and Bonding*, ed. X.-T. Wu and L. Chen, Spring, New York, Series ed. D. M. Mingos, 2012.
7 I. Chung and M. G. Kanatzidis, Metal Chalcogenides: A Rich Source of Nonlinear Optical Materials, *Chem. Mater.*, 2013, **26**, 849–869.
8 V. Petrov, Frequency down-conversion of solid-state laser sources to the mid-infrared spectral range using non-oxide nonlinear crystals, *Prog. Quantum Electron.*, 2015, **42**, 1–106.
9 A. Autere, H. Jussila, Y. Dai, Y. Wang, H. Lipsanen and Z. Sun, Nonlinear Optics with 2D Layered Materials, *Adv. Mater.*, 2018, **30**, e1705963.
10 P. S. Halasyamani and J. M. Rondinelli, The must-have and nice-to-have experimental and computational requirements for functional frequency doubling deep-UV crystals, *Nat. Commun.*, 2018, **9**, 2972.
11 A. Newell, *Nonlinear optics*, CRC Press, Boca Raton, 2018.
12 C. Wu, G. Yang, M. G. Humphrey and C. Zhang, Recent advances in ultraviolet and deep-ultraviolet second-order nonlinear optical crystals, *Coord. Chem. Rev.*, 2018, **375**, 459–488.
13 M. Mutailipu, M. Zhang, Z. Yang and S. Pan, Targeting the Next Generation of Deep-Ultraviolet Nonlinear Optical Materials: Expanding from Borates to Borate Fluorides to Fluorooxoborates, *Acc. Chem. Res.*, 2019, **52**, 791–801.
14 J. Chen, C. L. Hu, F. Kong and J. G. Mao, High-Performance Second-Harmonic-Generation (SHG) Materials: New Developments and New Strategies, *Acc. Chem. Res.*, 2021, **54**, 2775–2783.
15 W. Huang, S. Zhao and J. Luo, Recent Development of Non-π-Conjugated Deep Ultraviolet Nonlinear Optical Materials, *Chem. Mater.*, 2021, **34**, 5–28.
16 X. Chen and K. M. Ok, Metal oxyhalides: an emerging family of nonlinear optical materials, *Chem. Sci.*, 2022, **13**, 3942–3956.
17 L. Kang and Z. Lin, Deep-ultraviolet nonlinear optical crystals: concept development and materials discovery, *Light: Sci. Appl.*, 2022, **11**, 201.
18 Y. Li, J. Luo and S. Zhao, Local Polarity-Induced Assembly of Second-Order Nonlinear Optical Materials, *Acc. Chem. Res.*, 2022, **55**, 3460–3469.
19 Y. Xia, C. Chen, D. Tang and B. Wu, New nonlinear optical crystals for UV and VUV harmonic generation, *Adv. Mater.*, 1995, **7**, 79–81.
20 C. Chen, B. Wu, A. Jiang and G. You, A new-type ultraviolet SHG crystal β-BaB_2O_4, *Sci. China, Ser. B: Chem., Life Sci., Earth Sci.*, 1985, **28**, 235–243.
21 C. T. Chen, Y. C. Wu, A. D. Jiang, B. C. Wu, G. M. You, R. K. Li and S. J. Lin, New nonlinear-optical crystal: LiB_3O_5, *J. Opt. Soc. Am. B*, 1989, **6**, 616–621.
22 P. S. Peercy, "Soft" mode and coupled modes in the ferroelectric phase of KDP, *Solid State Commun.*, 1975, **16**, 439–442.
23 D. Z. Shen and C. Huang, A new nonlinear optical-crystal KTP, *Prog. Cryst. Growth Charact.*, 1985, **11**, 269–274.
24 A. Harasaki and K. Kato, New Data on the Nonlinear Optical Constant, Phase-Matching, and Optical Damage of $AgGaS_2$, *Jpn. J. Appl. Phys.*, 1997, **36**, 700–703.
25 G. C. Catella, L. R. Shiozawa, J. R. Hietanen, R. C. Eckardt, R. K. Route, R. S. Feigelson, D. G. Cooper and C. L. Marquardt, Mid-IR absorption in $AgGaSe_2$ optical parametric oscillator crystals, *Appl. Opt.*, 1993, **32**, 3948–3951.
26 G. D. Boyd, E. Buehler and F. G. Storz, Linear and nonlinear optical properties of ZnGeP2 and CdSe, *Appl. Phys. Lett.*, 1971, **18**, 301–304.
27 M. C. Ohmer, R. Pandey and B. H. Bairamov, Emergence of chalcopyrites as nonlinear optical materials, *MRS Bull.*, 1998, **23**, 16–20.
28 L. Bai, Z. Lin, Z. Wang, C. Chen and M. H. Lee, Mechanism of linear and nonlinear optical effects of chalcopyrite $AgGaX_2$ (X=S, Se, and Te) crystals, *J. Chem. Phys.*, 2004, **120**, 8772–8778.
29 L. Kang, M. Zhou, J. Yao, Z. Lin, Y. Wu and C. Chen, Metal Thiophosphates with Good Mid-infrared Nonlinear Optical Performances: A First-Principles Prediction and Analysis, *J. Am. Chem. Soc.*, 2015, **137**, 13049–13059.
30 S.-P. Guo, Y. Chi and G.-C. Guo, Recent achievements on middle and far-infrared second-order nonlinear optical materials, *Coord. Chem. Rev.*, 2017, **335**, 44–57.
31 F. Liang, L. Kang, Z. Lin, Y. Wu and C. Chen, Analysis and prediction of mid-IR nonlinear optical metal sulfides with diamond-like structures, *Coord. Chem. Rev.*, 2017, **333**, 57–70.
32 J.-R. Xiao, S.-H. Yang, F. Feng, H.-G. Xue and S.-P. Guo, A review of the structural chemistry and physical properties of metal chalcogenide halides, *Coord. Chem. Rev.*, 2017, **347**, 23–47.

33 M.-M. Chen, H.-G. Xue and S.-P. Guo, Multinary metal chalcogenides with tetrahedral structures for second-order nonlinear optical, photocatalytic, and photovoltaic applications, *Coord. Chem. Rev.*, 2018, **368**, 115–133.

34 P. Gong, F. Liang, L. Kang, X. Chen, J. Qin, Y. Wu and Z. Lin, Recent advances and future perspectives on infrared nonlinear optical metal halides, *Coord. Chem. Rev.*, 2019, **380**, 83–102.

35 L. Kang, F. Liang, X. Jiang, Z. Lin and C. Chen, First-Principles Design and Simulations Promote the Development of Nonlinear Optical Crystals, *Acc. Chem. Res.*, 2020, **53**, 209–217.

36 Q. G. Yue, W. B. Wei, H. Chen, X. T. Wu, H. Lin and Q. L. Zhu, Salt-inclusion chalcogenides: an emerging class of IR nonlinear optical materials, *Dalton Trans.*, 2020, **49**, 14338–14343.

37 L. Gao, J. Huang, S. Guo, Z. Yang and S. Pan, Structure-property survey and computer-assisted screening of mid-infrared nonlinear optical chalcohalides, *Coord. Chem. Rev.*, 2020, **421**, 213379.

38 H. D. Yang, M. Y. Ran, W. B. Wei, X. T. Wu, H. Lin and Q. L. Zhu, The Rise of Infrared Nonlinear Optical Pnictides: Advances and Outlooks, *Chem. – Asian J.*, 2021, **16**, 3299–3310.

39 H. Chen, M.-Y. Ran, W.-B. Wei, X.-T. Wu, H. Lin and Q.-L. Zhu, A comprehensive review on metal chalcogenides with three-dimensional frameworks for infrared nonlinear optical applications, *Coord. Chem. Rev.*, 2022, **470**, 214706.

40 H.-D. Yang, M.-Y. Ran, W.-B. Wei, X.-T. Wu, H. Lin and Q.-L. Zhu, Recent advances in IR nonlinear optical chalcogenides with well-balanced comprehensive performance, *Mater. Today Phys.*, 2023, **35**, 101127.

41 H. Lin, W.-B. Wei, H. Chen, X.-T. Wu and Q.-L. Zhu, Rational design of infrared nonlinear optical chalcogenides by chemical substitution, *Coord. Chem. Rev.*, 2020, **406**, 213150.

42 G. Zou and K. M. Ok, Novel ultraviolet (UV) nonlinear optical (NLO) materials discovered by chemical substitution-oriented design, *Chem. Sci.*, 2020, **11**, 5404–5409.

43 M.-Y. Ran, A.-Y. Wang, W.-B. Wei, X.-T. Wu, H. Lin and Q.-L. Zhu, Recent progress in the design of IR nonlinear optical materials by partial chemical substitution: structural evolution and performance optimization, *Coord. Chem. Rev.*, 2023, **481**, 215059.

44 H. Lin, L. Chen, L. J. Zhou and L. M. Wu, Functionalization based on the substitutional flexibility: strong middle IR nonlinear optical selenides $AX^{II}_4X^{III}_5Se_{12}$, *J. Am. Chem. Soc.*, 2013, **135**, 12914–12921.

45 S. P. Guo, X. Cheng, Z. D. Sun, Y. Chi, B. W. Liu, X. M. Jiang, S. F. Li, H. G. Xue, S. Deng, V. Duppel, J. Kohler and G. C. Guo, Large Second Harmonic Generation (SHG) Effect and High Laser-Induced Damage Threshold (LIDT) Observed Coexisting in Gallium Selenide, *Angew. Chem., Int. Ed.*, 2019, **58**, 8087–8091.

46 K. Wu, Y. Chu, Z. Yang and S. Pan, $A_2SrM^{IV}S_4$ (A=Li, Na; MIV=Ge, Sn) concurrently exhibiting wide bandgaps and good nonlinear optical responses as new potential infrared nonlinear optical materials, *Chem. Sci.*, 2019, **10**, 3963–3968.

47 H.-D. Yang, M.-Y. Ran, S.-H. Zhou, X.-T. Wu, H. Lin and Q.-L. Zhu, Rational Design via Dual-Site Aliovalent Substitution Leads to an Outstanding IR Nonlinear Optical Material with Well-Balanced Comprehensive Properties, *Chem. Sci.*, 2022, **13**, 10725–10733.

48 Q. Q. Liu, X. Liu, L. M. Wu and L. Chen, $SrZnGeS_4$: A Dual-Waveband Nonlinear Material With A Transparency Spanning UV-Vis and Far-IR Spectral Regions, *Angew. Chem., Int. Ed.*, 2022, **61**, e202205587.

49 M.-M. Chen, S.-H. Zhou, W.-B. Wei, X.-T. Wu, H. Lin and Q.-L. Zhu, Phase Matchability Transformation in the Infrared Nonlinear Optical Materials with Diamond-Like Frameworks, *Adv. Opt. Mater.*, 2022, **10**, 2102123.

50 P. Wang, Y. Chu, A. Tudi, C. Xie, Z. Yang, S. Pan and J. Li, The Combination of Structure Prediction and Experiment for the Exploration of Alkali-Earth Metal-Contained Chalcopyrite-Like IR Nonlinear Optical Material, *Adv. Sci.*, 2022, **9**, 2106120.

51 W. Cai, A. Abudurusuli, C. Xie, E. Tikhonov, J. Li, S. Pan and Z. Yang, Toward the Rational Design of Mid-Infrared Nonlinear Optical Materials with Targeted Properties via a Multi-Level Data–Driven Approach, *Adv. Funct. Mater.*, 2022, **32**, 2200231.

52 H. Chen, M.-Y. Ran, S.-H. Zhou, X.-T. Wu, H. Lin and Q.-L. Zhu, Simple yet extraordinary: super-polyhedra-built 3D chalcogenide framework of $Cs_5Ga_9S_{16}$ with excellent infrared nonlinear optical performance, *Chin. Chem. Lett.*, 2023, **34**, 107838.

53 M.-Y. Li, Z. Ma, B. Li, X.-T. Wu, H. Lin and Q.-L. Zhu, $HgCuPS_4$: An Exceptional Infrared Nonlinear Optical Material with Defect Diamond-like Structure, *Chem. Mater.*, 2020, **32**, 4331–4339.

54 H. Chen, Y.-Y. Li, B.-X. Li, P.-F. Liu, H. Lin, Q.-L. Zhu and X.-T. Wu, Salt-Inclusion Chalcogenide $[Ba_4Cl_2][ZnGa_4S_{10}]$: Rational Design of an IR Nonlinear Optical Material with Superior Comprehensive Performance Derived from $AgGaS_2$, *Chem. Mater.*, 2020, **32**, 8012–8019.

55 H. Chen, W.-B. Wei, H. Lin and X.-T. Wu, Transition-metal-based chalcogenides: A rich source of infrared nonlinear optical materials, *Coord. Chem. Rev.*, 2021, **448**, 214154.

56 C. Li, X. Meng, Z. Li and J. Yao, Hg-based chalcogenides: An intriguing class of infrared nonlinear optical materials, *Coord. Chem. Rev.*, 2022, **453**, 214328.

57 W. Zhou, J. Wu, W. Liu and S.-P. Guo, Ag-based chalcogenides and derivatives as promising infrared nonlinear optical materials, *Coord. Chem. Rev.*, 2023, **477**, 214950.

58 Y.-F. Shi, Y.-K. Chen, M.-C. Chen, L.-M. Wu, H. Lin, L.-J. Zhou and L. Chen, Strongest Second Harmonic Generation in the Polar R_3MTQ_7 Family: Atomic Distribution Induced Nonlinear Optical Cooperation, *Chem. Mater.*, 2015, **27**, 1876–1884.

59 Q. G. Yue, S. H. Zhou, B. Li, X. T. Wu, H. Lin and Q. L. Zhu, Quaternary Noncentrosymmetric Rare-Earth

Sulfides $Ba_4RE_2Cd_3S_{10}$ (RE=Sm, Gd, or Tb): A Joint Experimental and Theoretical Investigation, *Inorg. Chem.*, 2022, **61**, 1797–1804.

60 Z. X. Chen, C. Y. Zhao, X. H. Li, W. D. Yao, W. Liu and S. P. Guo, $KREP_2Se_6$ (RE=Sm, Gd, Tb): The First Rare-Earth Selenophosphates with Remarkable Nonlinear Optical Activities Realized by Synergistic Effect of RE- and P-Based Motifs, *Small*, 2023, **19**, e2206910.

61 M.-Y. Ran, S.-H. Zhou, W.-B. Wei, B.-X. Li, X.-T. Wu, H. Lin and Q.-L. Zhu, Rational Design of a Rare-Earth Oxychalcogenide $Nd_3[Ga_3O_3S_3][Ge_2O_7]$ with Superior Infrared Nonlinear Optical Performance, *Small*, 2023, **19**, 2300248.

62 M. C. Chen, L. M. Wu, H. Lin, L. J. Zhou and L. Chen, Disconnection enhances the second harmonic generation response: synthesis and characterization of $Ba_{23}Ga_8Sb_2S_{38}$, *J. Am. Chem. Soc.*, 2012, **134**, 6058–6060.

63 H. Lin, Y.-Y. Li, M.-Y. Li, Z. Ma, L.-M. Wu, X.-T. Wu and Q.-L. Zhu, Centric-to-acentric structure transformation induced by a stereochemically active lone pair: a new insight for design of IR nonlinear optical materials, *J. Mater. Chem. C*, 2019, **7**, 4638–4643.

64 M.-Y. Li, B. Li, H. Lin, Z. Ma, L.-M. Wu, X.-T. Wu and Q.-L. Zhu, $Sn_2Ga_2S_5$: A Polar Semiconductor with Exceptional Infrared Nonlinear Optical Properties Originating from the Combined Effect of Mixed Asymmetric Building Motifs, *Chem. Mater.*, 2019, **31**, 6268–6275.

65 Y. Xiao, M.-M. Chen, Y.-Y. Shen, P.-F. Liu, H. Lin and Y. Liu, $A_3Mn_2Sb_3S_8$ (A=K and Rb): A new type of multifunctional infrared nonlinear optical material based on unique three-dimensional open frameworks, *Inorg. Chem. Front.*, 2021, **8**, 2835–2843.

66 M. Yan, H.-G. Xue and S.-P. Guo, Recent Achievements in Lone-Pair Cation-Based Infrared SecondOrder Nonlinear Optical Materials, *Cryst. Growth Des.*, 2021, **21**, 698–720.

67 M.-M. Chen, Z. Ma, B.-X. Li, W.-B. Wei, X.-T. Wu, H. Lin and Q.-L. Zhu, $M_2As_2Q_5$ (M=Ba, Pb; Q=S, Se): a source of infrared nonlinear optical materials with excellent overall performance activated by multiple discrete arsenate anions, *J. Mater. Chem. C*, 2021, **9**, 1156–1163.

68 C. Liu, S.-H. Zhou, Y. Xiao, C. Zhang, H. Lin and Y. Liu, Aliovalent-cation-substitution-induced structure transformation: a new path toward high-performance IR nonlinear optical materials, *J. Mater. Chem. C*, 2021, **9**, 15407–15414.

69 X.-H. Li, Z.-H. Shi, M. Yang, W. Liu and S.-P. Guo, $Sn_7Br_{10}S_2$: The First Ternary Halogen-Rich Chalcohalide Exhibiting a Chiral Structure and Pronounced Nonlinear Optical Properties, *Angew. Chem., Int. Ed.*, 2022, **61**, e202115871.

70 M.-M. Chen, S.-H. Zhou, W. Wei, M.-Y. Ran, B. Li, X.-T. Wu, H. Lin and Q.-L. Zhu, $RbBiP_2S_6$: A Promising IR Nonlinear Optical Material with a Giant Second-Harmonic Generation Response Designed by Aliovalent Substitution, *ACS Mater. Lett.*, 2022, **4**, 1264–1269.

71 H.-J. Zhao, H.-D. Yang, P.-F. Liu and H. Lin, From *Cc* to $P6_3mc$: Structural Variation in $La_3S_2Cl_2[SbS_3]$ and $La_3OSCl_2[SbS_3]$ Induced by the Isovalent Anion Substitution, *Cryst. Growth Des.*, 2022, **22**, 1437–1444.

72 J. K. Harada, N. Charles, K. R. Poeppelmeier and J. M. Rondinelli, Heteroanionic Materials by Design: Progress Toward Targeted Properties, *Adv. Mater.*, 2019, **31**, 1805295.

73 Y.-Y. Li, W.-J. Wang, H. Wang, H. Lin and L.-M. Wu, Mixed-Anion Inorganic Compounds: A Favorable Candidate for Infrared Nonlinear Optical Materials, *Cryst. Growth Des.*, 2019, **19**, 4172–4192.

74 M.-Y. Ran, Z. Ma, H. Chen, B.-X. Li, X.-T. Wu, H. Lin and Q.-L. Zhu, Partial Isovalent Anion Substitution to Access Remarkable Second-Harmonic Generation Response: A Generic and Effective Strategy for Design of Infrared Nonlinear Optical Materials, *Chem. Mater.*, 2020, **32**, 5890–5896.

75 Y. F. Shi, W. B. Wei, X. T. Wu, H. Lin and Q. L. Zhu, Recent progress in oxychalcogenides as IR nonlinear optical materials, *Dalton Trans.*, 2021, **50**, 4112–4118.

76 M.-Y. Ran, S.-H. Zhou, B. Li, W. Wei, X.-T. Wu, H. Lin and Q.-L. Zhu, Enhanced Second-Harmonic-Generation Efficiency and Birefringence in Melillite Oxychalcogenides $Sr_2MGe_2OS_6$ (M=Mn, Zn, and Cd), *Chem. Mater.*, 2022, **34**, 3853–3861.

77 Y.-F. Shi, Z. Ma, B.-X. Li, X. Wu, H. Lin and Q.-L. Zhu, Phase matching achieved by isomorphous substitution in IR nonlinear optical material $Ba_2SnSSi_2O_7$ with an undiscovered $[SnO_4S]$ functional motif, *Mater. Chem. Front.*, 2022, **6**, 3054–3061.

78 Y. Zhang, H. Wu, Z. Hu and H. Yu, Oxychalcogenides: A Promising Class of Materials for Nonlinear Optical Crystals with Mixed-Anion Groups, *Chem. – Eur. J.*, 2023, **29**, e202203597.

79 Y. F. Shi, S. H. Zhou, B. Li, Y. Liu, X. T. Wu, H. Lin and Q. L. Zhu, $Ba_5Ga_2SiO_4S_6$: a Phase-Matching Nonlinear Optical Oxychalcogenide Design via Structural Regulation Originated from Heteroanion Introduction, *Inorg. Chem.*, 2023, **62**, 464–473.

80 J. Xu and K. Wu, Comprehensive review on multiple mixed-anion ligands, physicochemical performances and application prospects in metal oxysulfides, *Coord. Chem. Rev.*, 2023, **486**, 215139.

81 H.-D. Yang, S.-H. Zhou, M.-Y. Ran, X.-T. Wu, H. Lin and Q.-L. Zhu, Melillite oxychalcogenide $Sr_2FeGe_2OS_6$: a phase-matching IR nonlinear optical material realized by isomorphous substitution, *Inorg. Chem. Front.*, 2023, **10**, 2030–2038.

82 P. Wang, Y. Chu, A. Tudi, C. Xie, Z. Yang, S. Pan and J. Li, The Combination of Structure Prediction and Experiment for the Exploration of Alkali-Earth Metal-Contained Chalcopyrite-Like IR Nonlinear Optical Material, *Adv. Sci.*, 2022, **9**, 2106120.

83 J. Xiao, S. Zhu, B. Zhao, B. Chen, H. Liu and Z. He, Computational assessment of promising mid-infrared

nonlinear optical materials Mg–IV–V_2 (IV=Si, Ge, Sn; V=P, As): a first principles study, *Mater. Res. Express*, 2018, **5**, 035907.

84 K. E. Woo, J. Wang, K. Wu, K. Lee, J.-A. Dolyniuk, S. Pan and K. Kovnir, Mg-Si-As: An Unexplored System with Promising Nonlinear Optical Properties, *Adv. Funct. Mater.*, 2018, **28**, 1801589.

85 J. Chen, Q. N. Wu, H. Tian, X. Jiang, F. Xu, X. Zhao, Z. Lin, M. Luo and N. Ye, Uncovering a Vital Band Gap Mechanism of Pnictides, *Adv. Sci.*, 2022, **9**, 2105787.

86 A. Abudurusuli, J. Huang, P. Wang, Z. Yang, S. Pan and J. Li, $Li_4MgGe_2S_7$:TheFirst Alkali and Alkaline-Earth Diamond-Like Infrared Nonlinear Optical Material with Exceptional Large Band Gap, *Angew. Chem., Int. Ed.*, 2021, **60**, 24131–24136.

87 A. T. Barton, M. Liang, A. J. Craig, W. Zhang, S. S. Stoyko, A. N. Radzanowski, D. Fingerlow, P. S. Halasyamani, J. H. MacNeil and J. A. Aitken, $Li_2Mg_2Si_2S_6$ and $Li_2Mg_2Ge_2S_6$: Two nonlinear optical sulfides featuring a unique, polar trigonal structure incorporating ethane-like anions, *Z. Anorg. Allg. Chem.*, 2022, **648**, e202200071.

88 J. Chen, Y. Zhang, H. Wu, Z. Hu, J. Wang, Y. Wu and H. Yu, $AeMg_6Ga_6S_{16}$ (Ae=Ca, Sr, Ba): The First Double Alkaline Earth Metal Chalcogenides with Excellent Performances, *Adv. Opt. Mater.*, 2023, **11**, 2202147.

89 A. A. King, L. S. Breton, G. Morrison, M. D. Smith, M. Liang, P. S. Halasyamani and H.-C. zur Loye, Crystal Structures and Property Measurements of Rare Earth Magnesium Thiosilicates Synthesized via Flux Crystal Growth Utilizing the Boron Chalcogen Mixture (BCM) Method, *Inorg. Chem.*, 2023, **62**, 7446–7452.

90 H. Gao, K. Zhang, A. Abudurusuli, C. Bai, Z. Yang, K. Lai, J. Li and S. Pan, Syntheses, Structures and Properties of Alkali and Alkaline Earth Metal Diamond-Like Compounds Li_2MgMSe_4 (M=Ge, Sn), *Materials*, 2021, **14**, 6166.

91 K. Wu, Z. Yang and S. Pan, $Na_4MgM_2Se_6$ (M=Si, Ge): The First Noncentrosymmetric Compounds with Special Ethane-like $[M_2Se_6]^{6-}$ Units Exhibiting Large Laser Damage Thresholds, *Inorg. Chem.*, 2015, **54**, 10108–10110.

92 B.-W. Liu, M.-J. Zhang, Z.-Y. Zhao, H.-Y. Zeng, F.-K. Zheng, G.-C. Guo and J.-S. Huang, Synthesis, structure, and optical properties of the quaternary diamond-like compounds I_2–II–IV–VI_4 (I=Cu; II=Mg; IV=Si, Ge; VI=S, Se), *J. Solid State Chem.*, 2013, **204**, 251–256.

93 L. Luo, L. Wang, J. Chen, J. Zhou, Z. Yang, S. Pan and J. Li, $A^{I}B^{II}_3C^{III}_3Q^{VI}_8$: A New Family for the Design of Infrared Nonlinear Optical Materials by Coupling Octahedra and Tetrahedra Units, *J. Am. Chem. Soc.*, 2022, **144**, 21916–21925.

94 J. Chen, H. Chen, F. Xu, L. Cao, X. Jiang, S. Yang, Y. Sun, X. Zhao, C. Lin and N. Ye, $Mg_2In_3Si_2P_7$: A Quaternary Diamond-like Phosphide Infrared Nonlinear Optical Material Derived from $ZnGeP_2$, *J. Am. Chem. Soc.*, 2021, **143**, 10309–10316.

95 G. Cicirello, K. Wu and J. Wang, Synthesis, crystal structure, linear and nonlinear optical properties of quaternary sulfides $Ba_6(Cu_2X)Ge_4S_{16}$ (X=Mg, Mn, Cd), *J. Solid State Chem.*, 2021, **300**, 122226.

96 B. Ji, K. Wu, Y. Chen, F. Wang, A. J. Rossini, B. Zhang and J. Wang, $Ba_6(Cu_xZ_y)Sn_4S_{16}$ (Z=Mg, Mn, Zn, Cd, In, Bi, Sn): High Chemical Flexibility Resulting in Good Nonlinear-Optical Properties, *Inorg. Chem.*, 2022, **61**, 2640.

97 M. El-Hagary, M. Emam-Ismail, E. R. Shaaban, A. Al-Rashidi and S. Althoyaib, Composition, annealing and thickness dependence of structural and optical studies on $Zn_{1-x}Mn_xS$ nanocrystalline semiconductor thin films, *Mater. Chem. Phys.*, 2012, **132**, 581–590.

98 R. L. Gitzendanner, C. M. Spencer, F. J. DiSalvo, M. A. Pell and J. A. Ibers, Synthesis and structure of a new quaternary rare-earth sulfide, $La_6MgGe_2S_{14}$, and the related compound $La_6MgSi_2S_{14}$, *J. Solid State Chem.*, 1997, **131**, 399–404.

99 L. S. Breton, G. Morrison, M. R. Lacroix, P. S. Halasyamani and H.-C. zur Loye, Lanthanide thioborates, an emerging class of nonlinear optical materials, efficiently synthesized using the boronchalcogen mixture method, *Chem. Commun.*, 2022, **58**, 7992–7995.

100 G. A. Marking and M. G. Kanatzidis, The ethane-like $(Ge_2S_6)^{6-}$ and $(Si_2Se_6)^{6-}$ ligands bound to main-group metals in $Na_8Pb_2(Ge_2S_6)_2$, $Na_8Sn_2(Ge_2S_6)_2$, and $Na_8Pb_2(Si_2Se_6)_2$, *J. Alloys Compd.*, 1997, **259**, 122–128.

101 Y.-K. Lian, R.-A. Li, X. Liu, L.-M. Wu and L. Chen, $Sr_6(Li_2Cd)A_4S_{16}$ (A=Ge, Sn): How to Go beyond the Band Gap Limitation via Site-Specific Modification, *Cryst. Growth Des.*, 2020, **20**, 8084–8089.

102 R. Duan, H. Lin, Y. Wang, Y. Zhou and L. Wu, Non-centrosymmetric sulfides $A_2Ba_6MnSn_4S_{16}$ (A=Li, Ag): syntheses, structures and properties, *Dalton Trans.*, 2020, **49**, 5914–5920.